Article

Photo-thermal Tuning of Graphene Oxide Coated Integrated Optical Waveguides

David Moss

Optical Sciences Center, Swinburne University of Technology, Hawthorn, VIC 3122, Australia
dmoss@swin.edu.au

Abstract: We experimentally investigate power-sensitive photo-thermal tuning (PTT) of two-dimensional (2D) graphene oxide (GO) films coated on integrated optical waveguides. We measure the light power thresholds for reversible and permanent GO reduction in silicon nitride (SiN) waveguides integrated with 1 and 2 layers of GO. Raman spectra at different positions of a hybrid waveguide with permanently reduced GO are characterized, verifying the inhomogeneous GO reduction along the direction of light propagation through the waveguide. The differences between the PTT induced by a continuous-wave laser and a pulsed laser are also compared, confirming that the PTT mainly depend on the average input power. These results reveal interesting features for 2D GO films coated on integrated optical waveguides, which are of fundamental importance for the control and engineering of GO's properties in hybrid integrated photonic devices.

Keywords: 2D materials; integrated optics; photo-thermal changes; graphene oxide

1. Introduction

Graphene oxide (GO) is a two-dimensional (2D) material that has attracted significant interest because of its many attractive properties such as broadband photoluminescence [1, 2], high Kerr nonlinearity [3, 4], strong material anisotropy [5, 6], broadband light absorption [7, 8], and tunable material properties in wide ranges [9, 10]. In addition, with its facile fabrication processes, GO has a strong capability for large-scale manufacturable on-chip integration [6, 11, 12].

The incorporation of GO into integrated photonic devices has led to the birth of GO integrated photonics, which has become a very active and fast-growing field [13]. Integrated photonic devices incorporating GO films have been demonstrated for a range of applications, such as light absorbers [7, 8, 14], optical lenses and imaging devices [10, 11, 15], polarization-selective devices [6, 16], sensors [17, 18], and nonlinear optical devices [19-23].

Since GO can be converted to a reduced form with graphene-like properties under strong light irradiation or high temperature [24, 25], it has long been used as a precursor for the preparation of graphene [13, 26, 27]. Given the difference between the material properties of GO and reduced GO (rGO) [3, 11, 28], investigating the mechanisms and conditions for GO reduction in hybrid integrated photonic devices is of fundamental importance for applying this functional 2D material to integrated photonic devices [13, 29].

Previously, we observed power-sensitive photo-thermal changes in GO films coated on integrated photonic waveguides [19] and ring resonators [30] in nonlinear four-wave mixing experiments. In this paper, we provide a more detailed characterization for such changes arising from a range of effects such as photo-thermal reduction, thermal dissipation, and self-heating in GO layers. We experimentally investigate photo-thermal tuning (PTT) of 2D GO films coated on integrated optical waveguides. We measure the light power thresholds for reversible and permanent GO reduction in silicon nitride (SiN) waveguides integrated with 1 and 2 layers of GO. We identify three reduction stages according to the existence of reversible versus permanent reduction. Raman spectra at

different positions of a hybrid waveguide with permanently reduced GO film are also characterized, showing the inhomogeneous nature of GO reduction the direction of light propagation through the waveguide. Finally, we compare the PTT induced by a continuous-wave (CW) laser and a pulsed laser with the same average power, and observe negligible difference between them. This confirms that the PTT mainly depend on the average power rather than the peak power of input light. These results reveal interesting features for the reduction of GO induced by the photo-thermal changes, which are useful for controlling and engineering GO's material properties in hybrid integrated photonic devices.

2. Device design and fabrication

Figure 1a show a schematic illustration of a GO-coated SiN waveguide with a monolayer GO film. The bare SiN waveguide has a cross-section of 1.70 μm × 0.72 μm. A complementary metal-oxide-semiconductor (CMOS) compatible crack-free method [31-33] was utilized to fabricate the uncoated SiN waveguides. First, a two-step deposition of SiN films was achieved via low-pressure chemical vapor deposition (LPCVD) for strain management and crack prevention. Next, 248-nm deep ultraviolet lithography and $CF_4/CH_2F_2/O_2$ fluorine-based dry etching were employed for patterning the SiN waveguides. After that, a silica upper cladding was deposited using high-density plasma-enhanced chemical vapor deposition (HDP-PECVD), followed by opening a window on it down to the top surface of the SiN waveguides via lithography and dry etching processes. The window was located near the waveguide input to enable a relatively high optical power injected into the GO coated segment [34]. The length of the opened window was L_w = 1.4 mm. Finally, 2D layered GO films were coated onto the SiN waveguide by using a solution-based method that enabled transfer-free and layer-by-layer film coating, as reported previously [6, 11, 12, 35]. Compared to the cumbersome film transfer processes employed for the on-chip integration of other 2D materials such as graphene and TMDCs [36-38], our GO coating method is highly scalable, enabling the precise control of the GO layer number (i.e., film thickness), the ability to coat large-area films, and good film attachment onto integrated chips [11, 13]. The total length of the SiN waveguide was L = 2 cm. A micrograph of the fabricated device corresponding to **Figure 1a** is shown in **Figure 1b**. The GO film coated on the chip surface exhibited good morphology, high transmittance, and high uniformity. **Figure 1c** shows the schematic cross section of the hybrid waveguide in **Figure 1a**, the corresponding TE mode profile is shown in **Figure 1d**. The light-matter interaction between the waveguide evanescent field and the GO film can induce power-sensitive photo-thermal changes in the GO film, which has been observed previously [19, 29, 30]. In this paper, we only investigate PTT induced by the TE polarized light. This is because the TE polarization supports the in-plane interaction between the waveguide evanescent field and the 2D GO film, which is much stronger compared to the out-of-plane interaction given the significant anisotropy of 2D GO films [6], thus allowing for the excitation of higher levels of photo thermal changes.
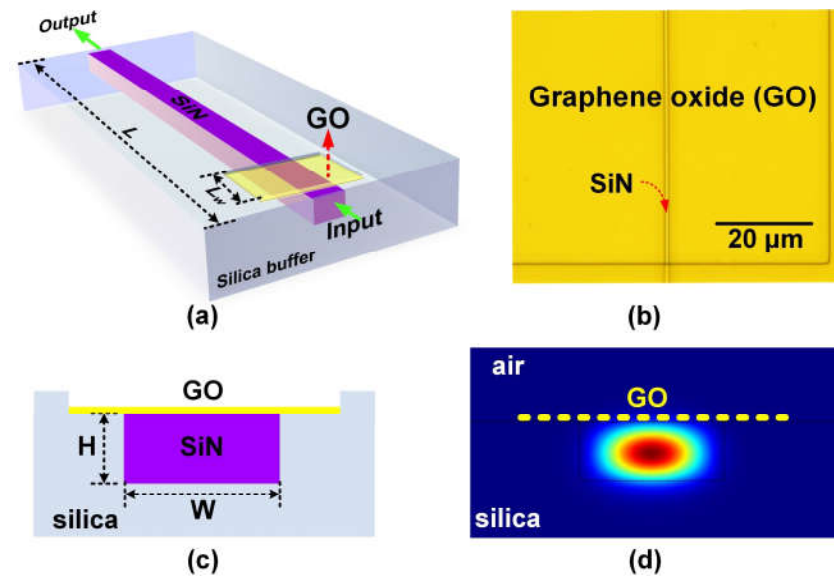
Figure 1. (a) Schematic illustration of a SiN waveguide coated with 1 layer of GO. (b) A micrograph showing the area around the opened window of the fabricated device corresponding to (a). (c) Schematic illustration of the cross-section of the hybrid waveguide. (d) TE mode profile corresponding to (c).

3. Experimental results

Figure 2 shows the experimental setup for characterizing PTT of GO films coated on integrated optical waveguides. Two CW light sources having different powers were employed. The low power one was used to measure the loss at low powers without obvious photo thermal changes in the GO films, whereas the high-power one was achieved by amplification with an erbium-doped fiber amplifier (EDFA) to excite the PTT. A pulsed laser source (repetition rate: 60 MHz, pulse width: 3.7 ps) was also employed to compare the level of photo thermal changes with that induced by the CW light. The wavelengths of both the CW sources and the center wavelength of the picosecond optical pulses were around 1550 nm. Polarization controllers (PCs) were employed to ensure the TE polarization of the input light. An optical isolator was inserted in the high-power light path to prevent the reflected light from damaging the light source. The input laser was split into two beams via a 50:50 beam splitter, with one injecting into the device under test (DUT) and the other being sent to an optical power meter (OPM) for monitoring the input power. Lensed fibers were used to butt couple light into and out of the DUT with a coupling loss of ~2 dB / facet. A charged-coupled device (CCD) camera was placed above the waveguide to monitor the adjusting of the coupling. Another OPM was employed to measure the output power after passing through the DUT.
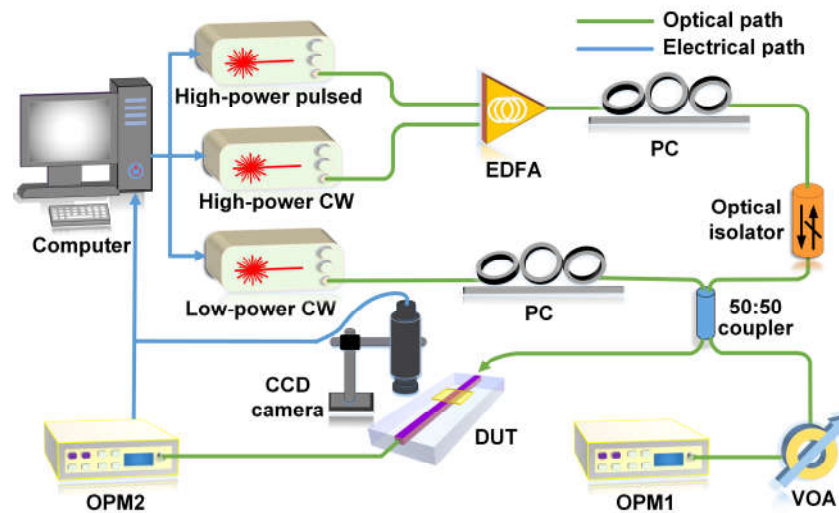
Figure 2. Experimental setup for characterization of PTT of GO-coated integrated waveguides. EDFA: erbium-doped fiber amplifier. PC: polarization controller. DUT: device under test. CCD: charged-coupled device. VOA: variable optical attenuator. OPM: optical power meter.

Figure 3a depicts the measured insertion loss of the integrated waveguide coated with 1 layer of GO versus input CW power. Unless otherwise specified, the input power of CW light or optical pulses in this paper represents the power coupled into the waveguide after subtracting the fiber-to-chip coupling loss. In order to characterize both the reversible and permanent changes of the material properties, after each measurement at a specific input power, we turned off the high-power CW light and remeasured the insertion loss using a low-power CW light with a power of 0 dBm. The results measured using the high-power and the low-power CW light sources are shown by the red and blue dots, respectively. As can be seen, the evolution of the PTT of the GO film can be divided into three reduction stages. At Stage I, when the input power was below 20 dBm, the insertion loss of the waveguide remained constant despite the increase in input power, reflecting that there was negligible change in the absorption of the GO film and the light power was not high enough to induce obvious photo-thermal changes. At Stage II starting from 20 dBm, the insertion loss showed a slight but observable increase with the input power, indicating the occurrence of the photo-thermal changes in the GO film. The results measured using low-power CW light after tuning off the high-power CW light remained constant. This reflects the fact that there were no permanent changes in the GO films, and the photo-thermal changes at this stage were reversible. These features of the photo-thermal changes in the GO films are consistent with previous reports [19, 34]. For Stage III, when the input power was further increased to above 22 dBm, the results measured using low-power CW light also showed an obvious increase with input power. Since permanently reduced GO films did not show any obvious power dependence [7, 8], this reflects the fact that there were permanent changes in the GO films. In addition, the difference between the red dots and their corresponding blue dots indicates that there was still reversibly reduced GO and only part of the GO film was permanently reduced. We infer that there would be a new stage after Stage III at even higher powers, where the difference between the red and blue dots at the same power would vanish due to the full reduction of all the GO films. We could not observe this stage in our experiments since we had already applied the maximum experimentally available power to the DUT.
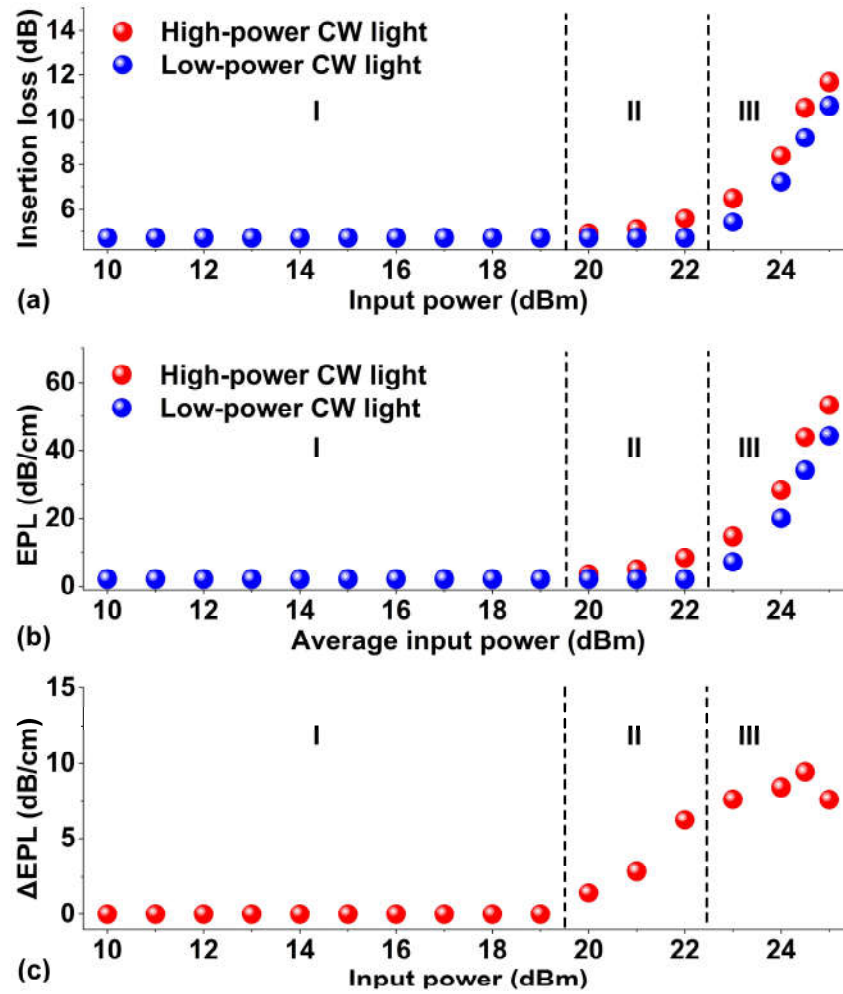
Figure 3. Experimental results for characterizing PTT of the hybrid waveguide coated with 1 layer of GO. (a) Insertion loss of the hybrid waveguide versus the input power of the high-power light source. The red dots show the loss of the high-power CW light source, and the blue dots show the loss measured with a low-power CW light source after exposure at the power level indicated on the x-axis. (b) GO-induced excess propagation loss (EPL) versus input power of the high-power light source. The red and blue dots show the results corresponding to the red and blue dots in (a), respectively. (c) ΔEPL extracted from (b) showing the difference between the red and blue dots.

Figure 3b depicts the GO-induced excess propagation loss (EPL) extracted from **Figure 3a**. The *EPL* (dB/cm) is defined as

$$EPL = (IL - IL_0)/L_w \tag{1}$$

where *IL* is the measured insertion loss of the hybrid waveguide in **Figure 3a**, IL_0 is the insertion loss of the bare waveguide, and L_w is the GO film length. **Figure 3c** shows the ΔEPL extracted from **Figure 3b**, which is defined as the difference between the red and blue dots after exposure by the high-power CW source at the input power indicated on the x-axis. As can be seen, the ΔEPL remained zero at Stage I, and started to increase at Stage II. In Stage III, the ΔEPL first slightly increased and then decreased when the input power was above 24 dBm. This can be attributed to the hybrid nature of GO films at this stage due to the co-existence of the permanently and reversibly reduced GO.
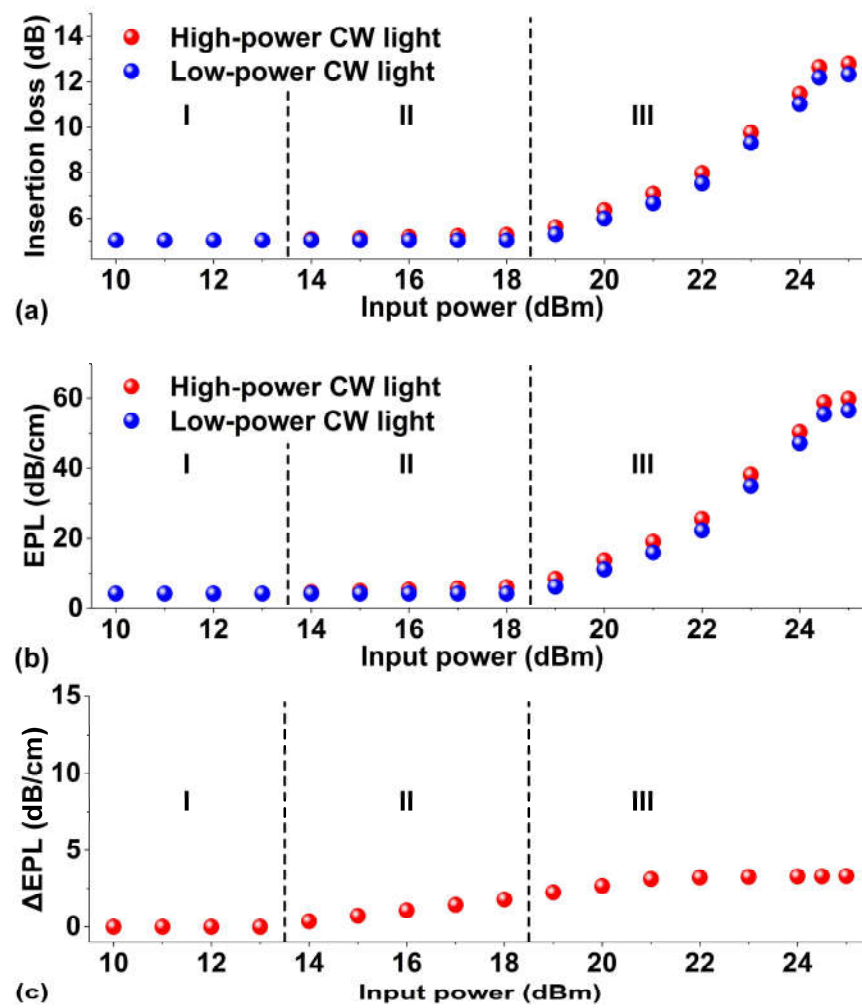
Figure 4. Experimental results for characterizing PTT of the hybrid waveguide coated with 2 layers of GO. (a) Insertion loss of the hybrid waveguide versus the input power of the high-power light source. The red dots show the loss of the high-power CW light source, and the blue dots show the loss measured with a low-power CW light source after exposure at the power level indicated on the x-axis. (b) GO-induced excess propagation loss (EPL) versus input power of the high-power light source. The red and blue dots show the results corresponding to the red and blue dots in (a), respectively. (c) ΔEPL extracted from (b) showing the difference between the red and blue dots.

The corresponding experimental results for the hybrid waveguide coated with 2 layers of GO are shown in **Figure 4**. **Figure 4a** shows the measured insertion loss versus input CW power. Similar to the results for the device with 1 layer of GO, the evolution of the PTT of the device with 2 layers of GO can also be divided into three reduction stages with increasing input power. Compared to the results in **Figure 3a**, the power thresholds for Stage II and Stage III were lower, with Stage II starting at 13 dBm and Stage III starting at 18 dBm. This reflects the fact that the power endurance of the film with 2 layers of GO was lower than the film with 1 layer of GO.

Figure 4b shows the GO induced EPL extracted from **Figure 4a**. Compared to the results in **Figure 3b**, the EPL here increased more slowly with input power. At Stage I, the excess propagation loss induced in the film with 2 layers of GO is about twice that induced in the film with a single layer of GO. However, at Stage II and Stage III, the difference between the EPL induced in 1 and 2 layers of GO became smaller, particularly at higher powers above 20 dBm. This is because the EPL defined in **Equation (1)** is a parameter averaged over the GO film length, whereas the reduction of GO in practical hybrid waveguides induced by the photo thermal changes is nonuniform, *i.e.*, the GO film at the beginning of the waveguide is more easily to be reduced, which absorbs more light power and so protects the GO film following it from being reduced. The film with 2 layers of GO

absorbed more light than the film with 1 layer of GO, and so the light transmission was more attenuated over a shorter distance, resulting in a higher proportion of unreduced GO. The loss of the non-reduced 2 layers of GO was lower than the single layer of rGO, thus resulting in a lower EPL.

Figure 4c shows the *ΔEPL* extracted from **Figure 4b**. Unlike the trend in **Figure 3c**, the *ΔEPL* here increases with input power in Stages II and III without showing obvious decrease. This is because for the hybrid waveguide with 2 layers of GO, only a small length of the GO film near the waveguide input was permanently reduced, leaving significant lengths of GO films that were either non-reduced or only reversibly reduced. Although the *ΔEPL* increased to above zero at relatively low input power for the device with 2 layers of GO, it increased more slowly with input power, with the values at high input powers being smaller than those for the device with 1 layer of GO. This is because for the film with 2 layers of GO, the reversibly reduced GO experienced relatively lower power (14 – 18 dBm), while the film exposed to higher power was permanently reduced and no longer exhibited *ΔEPL*. On the other hand, for the single layer GO film, the reversibly reduced GO experienced relatively higher powers (20 – 22 dBm), thus yielding a higher *ΔEPL*.

4. Discussion

In section 3, the inhomogeneous GO reduction along the hybrid waveguides was used to explain several experimental phenomena. To verify the inhomogeneous nature of the GO reduction induced by the photo thermal changes, we characterized the Raman spectra of 2 layers of GO coated on an integrated waveguide after applying the maximum input power of 24 dBm. The results are shown in **Figure 5**, where representative D and G peaks of GO can be clearly identified. Near the waveguide input, the D and G peaks of the detected Raman signals are relatively small, with a D/G ratio being larger than 1. This is similar to that of graphene [11], indicating that the GO film here was deeply reduced. In contrast, for positions further away from the waveguide input, the D/G ratio decreased to become less than 1, together with an increased intensity for the detected Raman signal. These characteristics show agreement with Raman spectra of GO having fewer defects [9, 12] and reflect the fact that the GO away from the waveguide input was reduced less.
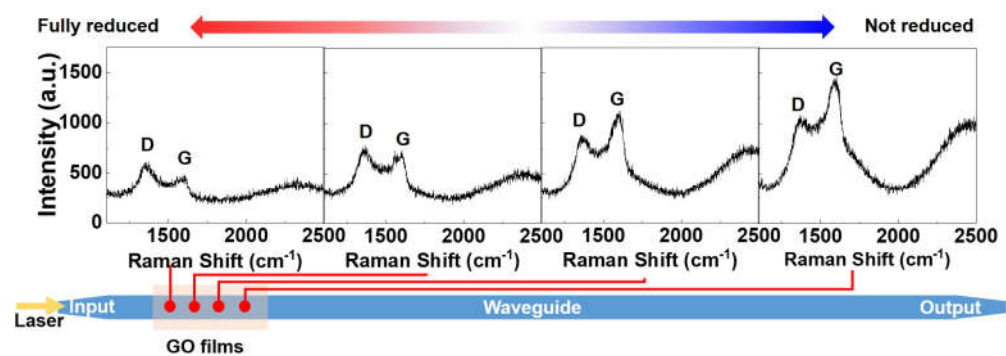

Figure 5. Raman spectra of 2 layers of GO coated on an integrated waveguide after applying an input CW power of 24 dBm.

To compare the PTT induced by CW light versus optical pulses, we measured the EPLs of the hybrid waveguides with a single GO layer for both CW light and optical pulses having the same average power. The results are shown in **Figure 6**. The optical pulses had a repetition rate of ~60 MHz and a pulse width of ~3.7 ps, which corresponded to a peak power 4×10^3 times higher than the CW light with the same average power. As can be seen, both the CW light and the optical pulses induced measurable EPLs at high average input powers. The small difference between them indicates that the EPL was mainly a function of the average power rather than peak power. This is in agreement with observations in GO films arising from photo-thermal processes in Refs. [19, 29, 30], and further confirms the existence of the photo thermal changes. In contrast, the changes

induced by ultrafast nonlinear optical processes such as four-wave mixing, two-photon absorption, and saturable absorption are dependent on the peak input light power [34, 39, 40]. The slightly lower EPL induced by optical pulses compared to CW light can be attributed to saturable absorption in the GO films caused by the high peak powers, which was also observed in Refs. [23, 41]. We also measured permanent EPLs with low-power CW light (0 dBm) after turning off the high-power CW light and optical pulses. The permanent EPLs induced by the CW and optical pulses showed negligible difference, reflecting the fact that the permanent reduction of GO was mainly induced by the photo thermal changes. These results have significant implications for designing and engineering nonlinear photonic chips for applications such as microcombs. [42-99]
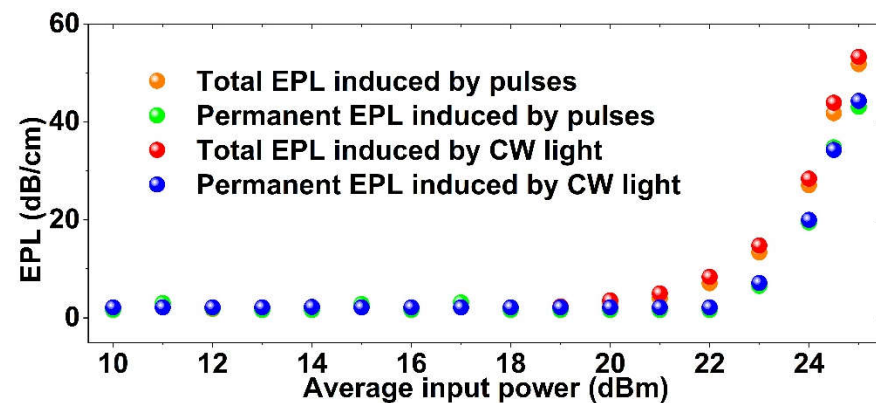

Figure 6. Experimental results of the total and permanent EPL induced by a CW light and optical pulses versus average input power for the hybrid waveguides coated with 1 layer of GO.

5. Conclusions

In this paper, we present detailed characterization of the PTT of GO films coated on integrated optical waveguides. Reversible and permanent GO reduction are observed by applying different CW laser powers to the devices with 1 and 2 layers of GO. The corresponding power thresholds are measured, with three reduction stages being identified. The Raman spectra at different positions of a hybrid waveguide with a permanently reduced GO film are characterized, which verifies the inhomogeneity of GO reduction. The photo-thermal changes induced by CW light and optical pulses with the same average power are also compared, which show negligible difference and confirms that the PTT mainly depends on the average input power. These results are useful for controlling and engineering the material properties of GO in hybrid integrated photonic devices.

Conflicts of Interest: The authors declare no conflict of interest.

References

1.   Chien, C.-T.; S.-S. Li; W.-J. Lai; Y.-C. Yeh; H.-A. Chen; I.-S. Chen; L.-C. Chen; K.-H. Chen; T. Nemoto; S. Isoda; et al. Tunable Photoluminescence from Graphene Oxide. *Angew. Chem. Int.* **2012**, 51, 6662-6666.

2.   Cushing, S.K.; M. Li; F. Huang; N. Wu Origin of strong excitation wavelength dependent fluorescence of graphene oxide. *ACS nano* **2014**, 8, 1002-1013.

3.   Zheng, X.R.; B.H. Jia; X. Chen; M. Gu In Situ Third-Order Nonlinear Responses During Laser Reduction of Graphene Oxide Thin Films Towards On-Chip Nonlinear Photonic Devices. *Adv. Mater.* **2014**, 26, 2699-2703.

4.   Xu, X.C.; X.R. Zheng; F. He; Z. Wang; H. Subbaraman; Y.G. Wang; B.H. Jia; R.T. Chen Observation of Third-order Nonlinearities in Graphene Oxide Film at Telecommunication Wavelengths. *Sci. Rep.* **2017**, 7.

5.   Lim, W.H.; Y.K. Yap; W.Y. Chong; C.H. Pua; N.M. Huang; R.M. De La Rue; H. Ahmad Graphene oxide-based waveguide polariser: From thin film to quasi-bulk. *Opt. Express* **2014**, 22, 11090-11098.

6.   Wu, J.Y.; Y.Y. Yang; Y. Qu; X.Y. Xu; Y. Liang; S.T. Chu; B.E. Little; R. Morandotti; B.H. Jia; D.J. Moss Graphene Oxide Waveguide and Micro-Ring Resonator Polarizers. *Laser Photonics Rev.* **2019**, 13.

7.   Lin, H.; B.C.P. Sturmberg; K.-T. Lin; Y. Yang; X. Zheng; T.K. Chong; C.M. de Sterke; B. Jia A 90-nm-thick graphene metamaterial for strong and extremely broadband absorption of unpolarized light. *Nat. Photonics* **2019**, 13, 270-276.

8.   Lin, K.-T.; H. Lin; T. Yang; B. Jia Structured graphene metamaterial selective absorbers for high efficiency and omnidirectional solar thermal energy conversion. *Nat. Commun.* **2020**, 11, 1389.

9.   Loh, K.P.; Q. Bao; G. Eda; M. Chhowalla Graphene oxide as a chemically tunable platform for optical applications. *Nat. Chem.* **2010**, 2, 1015-24.

10.   Zheng, X.; B. Jia; H. Lin; L. Qiu; D. Li; M. Gu Highly efficient and ultra-broadband graphene oxide ultrathin lenses with three-dimensional subwavelength focusing. *Nat. Commun.* **2015**, 6, 8433.

11.   Yang, Y.; H. Lin; B.Y. Zhang; Y. Zhang; X. Zheng; A. Yu; M. Hong; B. Jia Graphene-Based Multilayered Metamaterials with Phototunable Architecture for on-Chip Photonic Devices. *ACS Photonics* **2019**, 6, 1033-1040.

12.   Yang, Y.; J. Wu; X. Xu; Y. Liang; S.T. Chu; B.E. Little; R. Morandotti; B. Jia; D.J. Moss Invited Article: Enhanced four-wave mixing in waveguides integrated with graphene oxide. *APL Photonics* **2018**, 3, 120803.

13.   Wu, J.; L. Jia; Y. Zhang; Y. Qu; B. Jia; D.J. Moss Graphene Oxide for Integrated Photonics and Flat Optics. *Adv. Mater.* **2021**, 33, 2006415.

14.   Chen, X.; B. Jia; Y. Zhang; M. Gu Exceeding the limit of plasmonic light trapping in textured screen-printed solar cells using Al nanoparticles and wrinkle-like graphene sheets. *Light: Science & Applications* **2013**, 2, e92-e92.

15.   Cao, G.; H. Lin; S. Fraser; X. Zheng; B. Del Rosal; Z. Gan; S. Wei; X. Gan; B. Jia Resilient Graphene Ultrathin Flat Lens in Aerospace, Chemical, and Biological Harsh Environments. *ACS Appl. Mater. Interfaces* **2019**, 11, 20298-20303.

16.   Zheng, X.; B. Xu; S. Li; H. Lin; L. Qiu; D. Li; B. Jia Free-standing graphene oxide mid-infrared polarizers. *Nanoscale* **2020**, 12, 11480-11488.

17.   Leo Tsui, H.C.; O. Alsalman; B. Mao; A. Alodhayb; H. Albrithen; A.P. Knights; M.P. Halsall; I.F. Crowe Graphene oxide integrated silicon photonics for detection of vapour phase volatile organic compounds. *Sci. Rep.* **2020**, 10, 9592.

18.   He, S.; B. Song; D. Li; C. Zhu; W. Qi; Y. Wen; L. Wang; S. Song; H. Fang; C. Fan A Graphene Nanoprobe for Rapid, Sensitive, and Multicolor Fluorescent DNA Analysis. *Adv. Funct. Mater.* **2010**, 20, 453-459.

19.   Qu, Y.; J. Wu; Y. Yang; Y. Zhang; Y. Liang; H. El Dirani; R. Crochemore; P. Demongodin; C. Sciancalepore; C. Grillet; et al. Enhanced Four-Wave Mixing in Silicon Nitride Waveguides Integrated with 2D Layered Graphene Oxide Films. *Adv. Opt. Mater.* **2020**, n/a, 2001048.

20.   Zhang, Y.; J. Wu; Y. Yang; Y. Qu; L. Jia; T. Moein; B. Jia; D.J. Moss Enhanced Kerr Nonlinearity and Nonlinear Figure of Merit in Silicon Nanowires Integrated with 2D Graphene Oxide Films. *ACS Appl. Mater. Interfaces* **2020**, 12, 33094-33103.

21.   Zhang, Y.; J. Wu; Y. Qu; L. Jia; B. Jia; D.J. Moss Optimizing the Kerr Nonlinear Optical Performance of Silicon Waveguides Integrated With 2D Graphene Oxide Films. *J. Lightwave Technol.* **2021**, 39, 4671-4683.

22.   Zhang, Y.; J. Wu; Y. Yang; Y. Qu; L. Jia; B. Jia; D.J. Moss Enhanced Spectral Broadening of Femtosecond Optical Pulses in Silicon Nanowires Integrated with 2D Graphene Oxide Films. *Micromachines-Basel* **2022**, 13, 756.

23.   Zhang, Y.; J. Wu; Y. Yang; Y. Qu; H.E. Dirani; R. Crochemore; C. Sciancalepore; P. Demongodin; C. Grillet; C. Monat; et al. Enhanced self-phase modulation in silicon nitride waveguides integrated with 2D graphene oxide films. *IEEE J. Sel. Top. Quant.* **2022**, 1-1.

24.   Zhang, Y.-L.; L. Guo; H. Xia; Q.-D. Chen; J. Feng; H.-B. Sun Photoreduction of Graphene Oxides: Methods, Properties, and Applications. *Adv. Opt. Mater.* **2014**, 2, 10-28.

25.   Compton, O.C.; S.T. Nguyen Graphene oxide, highly reduced graphene oxide, and graphene: versatile building blocks for carbon-based materials. *Small* **2010**, 6, 711-23.

26.   Zhu, Y.; S. Murali; W. Cai; X. Li; J.W. Suk; J.R. Potts; R.S. Ruoff Graphene and Graphene Oxide: Synthesis, Properties, and Applications. *Adv. Mater.* **2010**, 22, 3906-3924.

27.   Brisebois, P.P.; M. Siaj Harvesting graphene oxide – years 1859 to 2019: a review of its structure, synthesis, properties and exfoliation. *J. Mater. Chem. C* **2020**, 8, 1517-1547.

28.   Pei, S.; H.-M. Cheng The reduction of graphene oxide. *Carbon* **2012**, 50, 3210-3228.

29.   Chong, W.Y.; W.H. Lim; Y.K. Yap; C.K. Lai; R.M. De La Rue; H. Ahmad Photo-induced reduction of graphene oxide coating on optical waveguide and consequent optical intermodulation. *Sci. Rep.* **2016**, 6, 23813.

30.   Wu, J.; Y. Yang; Y. Qu; L. Jia; Y. Zhang; X. Xu; S.T. Chu; B.E. Little; R. Morandotti; B. Jia; et al. 2D Layered Graphene Oxide Films Integrated with Micro-Ring Resonators for Enhanced Nonlinear Optics. *Small*, n/a, 1906563.

31.   El Dirani, H.; A. Kamel; M. Casale; S. Kerdiles; C. Monat; X. Letartre; M. Pu; L.K. Oxenløwe; K. Yvind; C. Sciancalepore Annealing-free Si3N4 frequency combs for monolithic integration with Si photonics. *Appl. Phys. Lett.* **2018**, 113, 081102.

32.   Demongodin, P.; H. El Dirani; J. Lhuillier; R. Crochemore; M. Kemiche; T. Wood; S. Callard; P. Rojo-Romeo; C. Sciancalepore; C. Grillet; et al. Ultrafast saturable absorption dynamics in hybrid graphene/Si3N4 waveguides. *APL Photonics* **2019**, 4, 076102.

33.   El Dirani, H.; L. Youssef; C. Petit-Etienne; S. Kerdiles; P. Grosse; C. Monat; E. Pargon; C. Sciancalepore Ultralow-loss tightly confining Si 3 N 4 waveguides and high-Q microresonators. *Opt. Express* **2019**, 27, 30726-30740.

34.   Qu, Y.; J. Wu; Y. Zhang; L. Jia; Y. Liang; B. Jia; D.J. Moss Analysis of Four-Wave Mixing in Silicon Nitride Waveguides Integrated With 2D Layered Graphene Oxide Films. *J. Lightwave Technol.* **2021**, 39, 2902-2910.

35.   Jia, L.; J. Wu; Y. Zhang; Y. Qu; B. Jia; Z. Chen; D.J. Moss Fabrication Technologies for the On-Chip Integration of 2D Materials. *Small Methods*, n/a, 2101435.

36.   Feng, Q.; H. Cong; B. Zhang; W. Wei; Y. Liang; S. Fang; T. Wang; J. Zhang Enhanced optical Kerr nonlinearity of graphene/Si hybrid waveguide. *Appl. Phys. Lett.* **2019**, 114, 071104.

37.   Liu, L.; K. Xu; X. Wan; J. Xu; C.Y. Wong; H.K. Tsang Enhanced optical Kerr nonlinearity of MoS2 on silicon waveguides. *Photonics Res.* **2015**, 3, 206-209.

38.   Yang, Y.; R. Liu; J. Wu; X. Jiang; P. Cao; X. Hu; T. Pan; C. Qiu; J. Yang; Y. Song Bottom-up fabrication of graphene on silicon/silica substrate via a facile soft-hard template approach. *Sci. Rep.* **2015**, 5, 1-7.

39.   Jiang, T.; V. Kravtsov; M. Tokman; A. Belyanin; M.B. Raschke Ultrafast coherent nonlinear nanooptics and nanoimaging of graphene. *Nat. Nanotechnol.* **2019**, 14, 838-843.

40.   Zhang, Y.; J. Wu; Y. Qu; L. Jia; B. Jia; D.J. Moss Design and Optimization of Four-Wave Mixing in Microring Resonators Integrated With 2D Graphene Oxide Films. *J. Lightwave Technol.* **2021**, 39, 6553-6562.

41.   Demongodin, P.; H. El Dirani; J. Lhuillier; R. Crochemore; M. Kemiche; T. Wood; S. Callard; P. Rojo-Romeo; C. Sciancalepore; C. Grillet; et al. Ultrafast saturable absorption dynamics in hybrid graphene/Si3N4 waveguides. *APL Photonics* **2019**, 4.

42.   M. Tan, X. Xu, J. Wu, T. G. Nguyen, S. T. Chu, B. E. Little, R. Morandotti, A. Mitchell, and D. J. Moss, "Orthogonally polarized Photonic Radio Frequency single sideband generation with integrated micro-ring resonators", IOP Journal of Semiconductors, Vol. 42 (4), 041305 (2021).

43.   C.Prayoonyong et al., "Frequency comb distillation for optical superchannel transmission", Journal of Lightwave Technology Vol. 39 (23) 7383-7392 (2021).

44.   X. Xu et al, "Photonic perceptron based on a Kerr microcomb for scalable high speed optical neural networks", Laser and Photonics Reviews, vol. 14, no. 8, 2000070 (2020).   DOI: 10.1002/lpor.202000070.

45.   X. Xu, et al., "11 TOPs photonic convolutional accelerator for optical neural networks", Nature 589, 44-51 (2021).

46.   Pasquazi, A. et al. Micro-combs: a novel generation of optical sources. Physics Reports 729, 1-81 (2018).

47.   Moss, D. J. et al., "New CMOS-compatible platforms based on silicon nitride and Hydex for nonlinear optics", Nature photonics 7, 597 (2013).

48.   B. Corcoran, et al., "Ultra-dense optical data transmission over standard fiber with a single chip source", Nature Communications, vol. 11, Article:2568, 2020.

49.   Kues, M. et al. Quantum optical microcombs. Nature Photonics 13, (3) 170-179 (2019). doi:10.1038/s41566-019-0363-0

50.   C. Reimer, L. Caspani, M. Clerici, et al., "Integrated frequency comb source of heralded single photons," Optics Express, vol. 22, no. 6, pp. 6535-6546, 2014.

51.   C. Reimer, et al., "Cross-polarized photon-pair generation and bi-chromatically pumped optical parametric oscillation on a chip", Nature Communications, vol. 6, Article 8236, 2015.   DOI: 10.1038/ncomms9236.

52.   L. Caspani, C. Reimer, M. Kues, et al., "Multifrequency sources of quantum correlated photon pairs on-chip: a path toward integrated Quantum Frequency Combs," Nanophotonics, vol. 5, no. 2, pp. 351-362, 2016.

53.   C. Reimer et al., "Generation of multiphoton entangled quantum states by means of integrated frequency combs," Science, vol. 351, no. 6278, pp. 1176-1180, 2016.

54.   M. Kues, et al., "On-chip generation of high-dimensional entangled quantum states and their coherent control", Nature, vol. 546, no. 7660, pp. 622-626, 2017.

55.   P. Roztocki et al., "Practical system for the generation of pulsed quantum frequency combs," Optics Express, vol. 25, no. 16, pp. 18940-18949, 2017.

56.   Y. Zhang, et al., "Induced photon correlations through superposition of two four-wave mixing processes in integrated cavities", Laser and Photonics Reviews, vol. 14, no. 7, pp. 2000128, 2020. DOI: 10.1002/lpor.202000128

57.   C. Reimer, et al.,"High-dimensional one-way quantum processing implemented on d-level cluster states", Nature Physics, vol. 15, no.2, pp. 148–153, 2019.

58.   Stern, B., Ji, X., Okawachi, Y., Gaeta, A. L. & Lipson, M. Battery-operated integrated frequency comb generator. Nature 562, 401 (2018).

59.   Bao, C., et al., Direct soliton generation in microresonators, Opt. Lett, 42, 2519 (2017).

60.   M.Ferrera et al., "CMOS compatible integrated all-optical RF spectrum analyzer", Optics Express, vol. 22, no. 18, 21488 - 21498 (2014).

61.   A. Pasquazi, et al., "Sub-picosecond phase-sensitive optical pulse characterization on a chip", Nature Photonics, vol. 5, no. 10, pp. 618-623 (2011).

62.   M. Kues, et al., "Passively modelocked laser with an ultra-narrow spectral width", Nature Photonics, vol. 11, no. 3, pp. 159, 2017.

63.   L. Razzari, et al., "CMOS-compatible integrated optical hyper-parametric oscillator," Nature Photonics, vol. 4, no. 1, pp. 41-45, 2010.

64.   M. Ferrera, et al., "Low-power continuous-wave nonlinear optics in doped silica glass integrated waveguide structures," Nature Photonics, vol. 2, no. 12, pp. 737-740, 2008.

65.   M.Ferrera et al."On-Chip ultra-fast 1st and 2nd order CMOS compatible all-optical integration", Opt. Express, vol. 19, (23)pp. 23153-23161 (2011).

66.   D. Duchesne, M. Peccianti, M. R. E. Lamont, et al., "Supercontinuum generation in a high index doped silica glass spiral waveguide," Optics Express, vol. 18, no, 2, pp. 923-930, 2010.

67.   H Bao, L Olivieri, M Rowley, ST Chu, BE Little, R Morandotti, DJ Moss, ... "Turing patterns in a fiber laser with a nested microresonator: Robust and controllable microcomb generation", Physical Review Research 2 (2), 023395 (2020).

68.   M. Ferrera, et al., "On-chip CMOS-compatible all-optical integrator", Nature Communications, vol. 1, Article 29, 2010.

69.   A. Pasquazi, et al., "All-optical wavelength conversion in an integrated ring resonator," Optics Express, vol. 18, no. 4, pp. 3858-3863, 2010.

70.   A. Pasquazi, Y. Park, J. Azana, et al., "Efficient wavelength conversion and net parametric gain via Four Wave Mixing in a high index doped silica waveguide," Optics Express, vol. 18, no. 8, pp. 7634-7641, 2010.

71.   M. Peccianti, M. Ferrera, L. Razzari, et al., "Subpicosecond optical pulse compression via an integrated nonlinear chirper," Optics Express, vol. 18, no. 8, pp. 7625-7633, 2010.

72.   Little, B. E. et al., "Very high-order microring resonator filters for WDM applications", IEEE Photonics Technol. Lett. 16, 2263–2265 (2004).

73.   M. Ferrera et al., "Low Power CW Parametric Mixing in a Low Dispersion High Index Doped Silica Glass Micro-Ring Resonator with Q-factor > 1 Million", Optics Express, vol.17, no. 16, pp. 14098–14103 (2009).

74.   M. Peccianti, et al., "Demonstration of an ultrafast nonlinear microcavity modelocked laser", Nature Communications, vol. 3, pp. 765, 2012.

75.   A. Pasquazi, et al., "Self-locked optical parametric oscillation in a CMOS compatible microring resonator: a route to robust optical frequency comb generation on a chip," Optics Express, vol. 21, no. 11, pp. 13333-13341, 2013.

76.   A. Pasquazi, et al., "Stable, dual mode, high repetition rate mode-locked laser based on a microring resonator," Optics Express, vol. 20, no. 24, pp. 27355-27362, 2012.

77.   Wu, J. et al. RF Photonics: An Optical Microcombs' Perspective. IEEE Journal of Selected Topics in Quantum Electronics Vol. 24, 6101020, 1-20 (2018).

78.   Xu, X., et al., Photonic microwave true time delays for phased array antennas using a 49 GHz FSR integrated micro-comb source, Photonics Research, 6, B30-B36 (2018).

79.   T. G. Nguyen et al., "Integrated frequency comb source-based Hilbert transformer for wideband microwave photonic phase analysis," Opt. Express, vol. 23, no. 17, pp. 22087-22097, Aug. 2015.

80.   X. Xu, J. Wu, M. Shoeiby, T. G. Nguyen, S. T. Chu, B. E. Little, R. Morandotti, A. Mitchell, and D. J. Moss, "Reconfigurable broadband microwave photonic intensity differentiator based on an integrated optical frequency comb source," APL Photonics, vol. 2, no. 9, 096104, Sep. 2017.

81.   X. Xu, M. Tan, J. Wu, R. Morandotti, A. Mitchell, and D. J. Moss, "Microcomb-based photonic RF signal processing", IEEE Photonics Technology Letters, vol. 31 no. 23 1854-1857, 2019.

82.   X. Xu, et al., "Broadband RF channelizer based on an integrated optical frequency Kerr comb source," Journal of Lightwave Technology, vol. 36, no. 19, pp. 4519-4526, 2018.

83.   X. Xu, et al., "Continuously tunable orthogonally polarized RF optical single sideband generator based on micro-ring resonators," Journal of Optics, vol. 20, no. 11, 115701. 2018.

84.   X. Xu, et al., "Orthogonally polarized RF optical single sideband generation and dual-channel equalization based on an integrated microring resonator," Journal of Lightwave Technology, vol. 36, no. 20, pp. 4808-4818. 2018.

85.   M.Tan, X. Xu, J. Wu, B. Corcoran, A. Boes, T. G. Nguyen, Sai T. Chu, B. E. Little, R.Morandotti, A. Mitchell, and D. J. Moss, "Integral order photonic RF signal processors based on a soliton crystal micro-comb source", IOP Journal of Optics vol. 23 (11) 125701 (2021).

86.   X. Xu, et al., "Advanced adaptive photonic RF filters with 80 taps based on an integrated optical micro-comb source," Journal of Lightwave Technology, vol. 37, no. 4, pp. 1288-1295, 2019.

87.   X. Xu, et al., "Broadband photonic RF channelizer with 90 channels based on a soliton crystal microcomb", Journal of Lightwave Technology, Vol. 38, no. 18, pp. 5116 - 5121, 2020. doi: 10.1109/JLT.2020.2997699.

88.   X. Xu, et al., "Photonic RF and microwave integrator with soliton crystal microcombs", IEEE Transactions on Circuits and Systems II: Express Briefs, vol. 67, no. 12, pp. 3582-3586, 2020. DOI:10.1109/TCSII.2020.2995682.

89.   X. Xu, et al., "Photonic RF phase-encoded signal generation with a microcomb source", J. Lightwave Technology, vol. 38, no. 7, 1722-1727, 2020.

90.   X. Xu, et al., "High performance RF filters via bandwidth scaling with Kerr micro-combs," APL Photonics, vol. 4, no. 2, pp. 026102. 2019.

91.   M. Tan, et al., "Microwave and RF photonic fractional Hilbert transformer based on a 50 GHz Kerr micro-comb", Journal of Lightwave Technology, vol. 37, no. 24, pp. 6097 – 6104, 2019.

92.   M. Tan, et al., "RF and microwave fractional differentiator based on photonics", IEEE Transactions on Circuits and Systems: Express Briefs, vol. 67, no.11, pp. 2767-2771, 2020. DOI:10.1109/TCSII.2020.2965158.

93.   M. Tan, et al., "Photonic RF arbitrary waveform generator based on a soliton crystal micro-comb source", Journal of Lightwave Technology, vol. 38, no. 22, pp. 6221-6226, Oct 22. 2020. DOI: 10.1109/JLT.2020.3009655.

94.   M. Tan, X. Xu, J. Wu, R. Morandotti, A. Mitchell, and D. J. Moss, "RF and microwave high bandwidth signal processing based on Kerr Micro-combs", Advances in Physics X, VOL. 6, NO. 1, 1838946 (2021). DOI:10.1080/23746149.2020.1838946.

95.   X. Xu, et al., "Advanced RF and microwave functions based on an integrated optical frequency comb source," Opt. Express, vol. 26 (3) 2569 2018.

96.   Xu, X., et al., Photonic microwave true time delays for phased array antennas using a 49 GHz FSR integrated micro-comb source, Photonics Research, 6, B30-B36 (2018).

97.   X. Xu, M. Tan, J. Wu, R. Morandotti, A. Mitchell, and D. J. Moss, "Microcomb-based photonic RF signal processing", IEEE Photonics Technology Letters, vol. 31 no. 23 1854-1857, 2019.

98.   M. Tan et al, "Orthogonally polarized Photonic Radio Frequency single sideband generation with integrated micro-ring resonators", IOP Journal of Semiconductors, Vol. 42 (4), 041305 (2021). DOI: 10.1088/1674-4926/42/4/041305.

99.   Maxwell Rowley, Pierre-Henry Hanzard, Antonio Cutrona, Hualong Bao, Sai T. Chu, Brent E. Little, Roberto Morandotti, David J. Moss, Gian-Luca Oppo, Juan Sebastian Totero Gongora, Marco Peccianti and Alessia Pasquazi, "Self- Emergence of Robust Micro Cavity-Solitons", Research Square (2022). DOI: 10.21203/rs.3.rs-468461/v1